Generation of propagating electron vortex states in photodetachment of H^-

F. Cajiao Vélez,* J. Z. Kamiński,† and K. Krajewska‡
Institute of Theoretical Physics, Faculty of Physics, University of Warsaw, Pasteura 5, 02-093 Warsaw, Poland

(Received 29 January 2020; accepted 27 April 2020; published 21 May 2020)

Generation of propagating electron vortex states in ionization of H^- by short, circularly polarized laser pulses is studied within the strong-field approximation. The latter, being particularly suitable for treating negative ions, is shown to be gauge independent for an *s*-electron system like H^-. Most importantly, it is demonstrated that the orbital angular momentum from the laser field can be efficiently transferred to photoelectrons, thus resulting in high orbital angular momenta electron vortex states. The conditions for this to happen are formulated and visualized with the help of coarse-grained probability distributions of photoelectrons, which are calculated by Monte Carlo method.

DOI: 10.1103/PhysRevA.101.053430

I. INTRODUCTION

Since the first experimental observation of propagating *electron vortex states* (EVSs) [1,2], an increasing amount of attention has been paid to their generation and manipulation. They have found numerous applications in electron microscopy, modern spectroscopic techniques, mechanical control of nanostructures, and many other fields [3,4]. EVSs are characterized by helixlike wave fronts with a vanishing probability at the helical axis. However, their most attractive feature is a nonzero (and quantized) orbital angular momentum (OAM) equal to $\hbar M$ (M is the so-called *topological charge* or *winding number*). In general, nonrelativistic propagating vortex states are special solutions of the field-free Schrödinger equation with a well-defined OAM; they are simultaneous eigenstates of the field-free Hamiltonian and the orbital angular momentum operator. Due to their axial symmetry, it becomes natural to analyze EVSs in cylindrical coordinates. Under those conditions, the Schrödinger equation accepts two types of solutions, the *Bessel* states and the *Laguerre-Gaussian* states. All those topics have been discussed in review articles [3,4], and the most relevant references are cited there.

We note that standard techniques of generating EVSs include the propagation of electron wave packets through spiral plates or gratings and by the action of magnetic monopoles upon electron beams [3,4]. However, it has been predicted that electron Bessel states of large angular momentum (topological charges up to thousands of units of $\hbar$) can be obtained in the strong-field photoionization of neutral atoms driven by short and intense laser pulses [5,6]. In this paper we shall investigate the generation of EVSs in photodetachment from atomic anions [7] (in particular, from H^-) by light pulses comprising only a few cycles.

The theoretical complexity of studying above-threshold detachment (ATD) from negative ions is reduced compared to that of studying above-threshold ionization from neutral atoms. This is because of the lack of long-range Coulomb interaction between the freed electron and its parent atom. Since short-range or zero-range potentials (ZRPs) are used to model negative ions (see, e.g., Refs. [8–18] and the review in [19]), the application of strong-field approximation (SFA) [20–22] to ATD is fully justified [23,24]. The drawback of the SFA is, however, that it is not gauge invariant. Hence, important discrepancies between length and velocity gauges are expected to appear, especially at high intensities of the driving laser field [25]. We show, however, that, when a ZRP model is used, the SFA leads to gauge-invariant results, as predicted by Gribakin and Kuchiev [23].

Based on the treatment developed by Gribakin and Kuchiev [23], we analyze here the electron photodetachment from H^- driven by ultrashort and circularly polarized laser pulses. While our method makes use of the strong-field approximation, the electron interaction with the neutral core is modeled as a ZRP. For the sake of comparison, we present some of our results in both velocity and length gauges. In particular, we explore the possibility of obtaining EVSs with a large topological charge in ATD. For our numerical illustrations we chose two light fields of different frequencies; we explore photodetachment driven by a CO_2 laser pulse (carrier frequency $\omega_L = 0.117\,\text{eV}$) and by a terahertz (THz) field ($\omega_L = 0.01\,\text{eV}$). Hence, the results presented here can be used not only for the analysis of ATD from a gas of negative ions but also to study the interactions of low-frequency laser fields with negative impurities doped in solid materials or at surfaces. Following this line of ideas, it would be, in principle, possible to generate propagating EVSs in solids. This could open a new field of research where the conduction properties of electrons are governed not only by their charge and spin (which are usually considered in spintronics [26]) but, additionally, by their orbital angular momentum.

This paper is organized as follows. In Sec. II we present the basis of the strong-field approximation for laser-induced photodetachment from negative ions. While in Secs. II A and

*Felipe.Cajiao-Velez@fuw.edu.pl
†Jerzy.Kaminski@fuw.edu.pl
‡Katarzyna.Krajewska@fuw.edu.pl

II B we derive general expressions for the probability amplitudes of ATD in the velocity and length gauges, in Sec. II C we restrict our attention to photodetachment from the $1s$ state of H^- within the ZRP model. Our treatment, in the length gauge, is similar to the one presented by Gribakin and Kuchiev [23]. However, the integral in time defining the probability amplitude of detachment is calculated numerically, instead of by means of the saddle-point approximation. The properties of the laser pulses considered for our numerical illustrations are established in Sec. III. In Sec. III A we extend the concept of *spiral of ionization* in momentum space [27–29] to photodetachment by ultrashort laser pulses. The energy spectra of photoelectrons, the coarse-grained probability distribution (CGPD), and their relationship with the spiral of ionization are presented in Secs. III B and III C. We also calculate the total probability of detachment by Monte Carlo methods there. The conditions necessary for the generation of propagating electron vortex states in ATD are elucidated in Sec. IV. Section IV A concerns the orbital angular momentum distributions of EVSs. Finally, our conclusions and perspectives are summarized in Sec. V.

Throughout the paper we set $\hbar = 1$, but we present the electron mass m_e and charge ($e < 0$) explicitly. Unless stated otherwise, in our numerical illustrations we use atomic units ($\hbar = m_e = |e| = 1$). Furthermore, in these units the speed of light is $c = 1/\alpha$, where α is the fine-structure constant.

II. PROBABILITY AMPLITUDE OF DETACHMENT

Consider a negatively charged ion interacting with a short laser pulse. Prior to that interaction ($t < 0$), the outermost electron is assumed to be in the unperturbed bound state $|\Phi_0\rangle$. In other words, $|\Phi_0\rangle$ is an eigenstate of the ionic Hamiltonian $\hat{H}_{\rm Ion}$ with eigenvalue E_0, i.e.,

$$E_0|\Phi_0\rangle = \hat{H}_{\rm Ion}|\Phi_0\rangle, \tag{1}$$

where

$$\hat{H}_{\rm Ion} = \frac{\hat{\boldsymbol{p}}^2}{2m_e} + W(\hat{\boldsymbol{r}}), \tag{2}$$

$\hat{\boldsymbol{p}}$ is the momentum operator, and $W(\hat{\boldsymbol{r}})$ is the binding potential energy. As $|\Phi_0\rangle$ is a stationary state, the time evolution operator corresponding to the Hamiltonian (2) $\hat{U}_{\rm Ion}(t,t')$ is given by

$$\hat{U}_{\rm Ion}(t,t') = e^{-i\hat{H}_{\rm Ion}(t-t')}, \quad t \geqslant t'. \tag{3}$$

In particular, we set our initial conditions such that, at time t, the electron is found in the state

$$|\Phi_0(t)\rangle = \lim_{t'\to-\infty} \hat{U}_{\rm Ion}(t,t')|\Phi_0(t')\rangle = e^{-iE_0 t}|\Phi_0\rangle. \tag{4}$$

In the presence of the light field, the total Hamiltonian $\hat{H}(t)$ governing the evolution of the system includes the electron interaction with the binding potential and the electromagnetic radiation, namely,

$$\hat{H}(t) = \hat{H}_{\rm Ion} + \hat{H}_{\rm I}(t) = \frac{\hat{\boldsymbol{p}}^2}{2m_e} + \hat{H}_{\rm I}(t) + W(\hat{\boldsymbol{r}}), \tag{5}$$

where $\hat{H}_{\rm I}(t)$, the interaction Hamiltonian, is gauge dependent. Specifically, as we are considering a finite laser pulse (duration T_p), it is assumed that $\hat{H}_{\rm I}(t) = 0$ for $t \leqslant 0$ and $t \geqslant T_p$.

The probability amplitude of electron detachment $\mathcal{A}(\boldsymbol{p})$ (from its bound state to the scattering state with asymptotic momentum $\boldsymbol{p}$) can be calculated by making use of the time evolution operator $\hat{U}(t,t')$ associated with the full Hamiltonian (5) (see, e.g., Ref. [5]),

$$\mathcal{A}(\boldsymbol{p}) = \lim_{t'\to-\infty}\lim_{t\to\infty} \mathcal{A}(\boldsymbol{p};t,t'), \tag{6}$$

where

$$\mathcal{A}(\boldsymbol{p};t,t') = \langle \boldsymbol{p}|\hat{U}(t,t')|\Phi_0\rangle \tag{7}$$

and $|\boldsymbol{p}\rangle$ is the eigenstate of the momentum operator such that $\langle \boldsymbol{p}|\boldsymbol{r}\rangle = e^{-i\boldsymbol{p}\cdot\boldsymbol{r}}$, i.e., it represents a field-free electron plane wave. Introducing now the Lippmann-Schwinger equation,

$$\hat{U}(t,t') = \hat{U}_{\rm Ion}(t,t') - i\int d\tau \hat{U}(t,\tau)\hat{H}_{\rm I}(\tau)\hat{U}_{\rm Ion}(\tau,t'), \tag{8}$$

we obtain

$$\mathcal{A}(\boldsymbol{p}) = -i\lim_{t\to\infty}\int_0^{T_p} d\tau \langle \boldsymbol{p}|\hat{U}(t,\tau)\hat{H}_{\rm I}(\tau)|\Phi_0(\tau)\rangle, \tag{9}$$

where Eq. (4) was used. Moreover, we define the photoelectron final scattering state,

$$\langle \Psi_{\boldsymbol{p}}(t)| = \langle \boldsymbol{p}|\hat{U}(\infty,t), \tag{10}$$

which, in principle, accounts for the presence of both the binding potential and the laser field. However, for negatively charged ions, the attractive potential exerted by the residual core decreases very fast with distance. For this reason, the exact scattering state can be approximated by a Volkov state [30] in the laser field, $|\Psi_{\boldsymbol{p}}(t)\rangle \approx |\psi_{\boldsymbol{p}}(t)\rangle$. This substitution is the essence of the strong-field approximation. Thus, the probability of photodetachment (9) takes the form

$$\begin{aligned}\mathcal{A}(\boldsymbol{p}) =& -i\int_0^{T_p} dt \langle \Psi_{\boldsymbol{p}}(t)|\hat{H}_{\rm I}(t)|\Phi_0(t)\rangle \\ \approx& -i\int_0^{T_p} dt \langle \psi_{\boldsymbol{p}}(t)|\hat{H}_{\rm I}(t)|\Phi_0(t)\rangle.\end{aligned} \tag{11}$$

It is worth mentioning that, similar to the interaction Hamiltonian, the Volkov solution is also gauge dependent. Therefore, in the following section we shall introduce the superscripts V and L to distinguish between the calculations in the velocity and length gauges, respectively. [Those two gauges are frequently used in the literature, although other forms of the gauge-dependent interaction $H_{\rm I}(t)$ are also conceivable.]

A. Velocity gauge

The probability amplitude of detachment in the velocity gauge is given by

$$\mathcal{A}^V(\boldsymbol{p}) = -i\int_0^{T_p} dt \langle \psi_{\boldsymbol{p}}^V(t)|\hat{H}_{\rm I}^V(t)|\Phi_0(t)\rangle. \tag{12}$$

In this case,

$$\hat{H}_{\rm I}^V(t) = -\frac{e}{m_e}\boldsymbol{A}(t)\cdot\hat{\boldsymbol{p}} + \frac{e^2}{2m_e}\boldsymbol{A}^2(t), \tag{13}$$

where $\boldsymbol{A}(t)$ is the vector potential defining the laser pulse. On the other hand, the Volkov solution $|\psi_{\boldsymbol{p}}^{V}(t)\rangle$ is defined as

$$|\psi_{\boldsymbol{p}}^{V}(t)\rangle = |\boldsymbol{p}\rangle \exp\left\{-i\frac{\boldsymbol{p}^2}{2m_e}t + \frac{i}{m_e}\int_0^t dt'\left[e\boldsymbol{A}(t')\cdot\boldsymbol{p} - \frac{e^2\boldsymbol{A}^2(t')}{2}\right]\right\}. \tag{14}$$

Inserting Eqs. (13) and (14) into Eq. (12), we find that the probability amplitude of detachment in the velocity gauge equals

$$\mathcal{A}^{V}(\boldsymbol{p}) = -i\int_0^{T_p} dt\,\tilde{\Phi}_0(\boldsymbol{p})\left(-\frac{e}{m_e}\boldsymbol{A}(t)\cdot\boldsymbol{p} + \frac{e^2}{2m_e}\boldsymbol{A}^2(t)\right)\exp\left\{i\left[\frac{\boldsymbol{p}^2}{2m_e} - E_0\right]t - \frac{i}{m_e}\int_0^t dt'\left[e\boldsymbol{A}(t')\cdot\boldsymbol{p} - \frac{e^2\boldsymbol{A}^2(t')}{2}\right]\right\}. \tag{15}$$

Here, we have introduced the Fourier transform of the bound state $\tilde{\Phi}_0(\boldsymbol{p}) = \langle\boldsymbol{p}|\Phi_0\rangle$, which will be explicitly calculated in Sec. II C.

B. Length gauge

As a consequence of the substitution of the exact scattering state by the Volkov solution, the expressions for the probability amplitude of detachment differ when calculated in different gauges and may lead to dissimilar predictions. For this reason we also present here the results corresponding to the length gauge. The probability amplitude reads

$$\mathcal{A}^{L}(\boldsymbol{p}) = -i\int_0^{T_p} dt\langle\psi_{\boldsymbol{p}}^{L}(t)|\hat{H}_{\mathrm{I}}^{L}(t)|\Phi_0(t)\rangle. \tag{16}$$

The interaction Hamiltonian now takes the form

$$\hat{H}_{\mathrm{I}}^{L}(t) = -e\boldsymbol{\mathcal{E}}(t)\cdot\hat{\boldsymbol{r}}, \tag{17}$$

where $\boldsymbol{\mathcal{E}}(t) = -\partial_t\boldsymbol{A}(t)$ is the oscillating electric field and $\hat{\boldsymbol{r}}$ is the position operator. In this gauge, the Volkov solution is given by

$$|\psi_{\boldsymbol{p}}^{L}(t)\rangle = |\boldsymbol{p} - e\boldsymbol{A}(t)\rangle \exp\left\{-i\frac{\boldsymbol{p}^2}{2m_e}t + \frac{i}{m_e}\int_0^t dt'\left[e\boldsymbol{A}(t')\cdot\boldsymbol{p} - \frac{e^2\boldsymbol{A}^2(t')}{2}\right]\right\}. \tag{18}$$

Therefore, from Eqs. (16), (17), and (18) we obtain the probability amplitude of photodetachment in the length gauge,

$$\mathcal{A}^{L}(\boldsymbol{p}) = ie\int_0^{T_p} dt\,\boldsymbol{\mathcal{E}}(t)\cdot\tilde{\boldsymbol{\Phi}}[\boldsymbol{p} - e\boldsymbol{A}(t)]\exp\left\{i\left[\frac{\boldsymbol{p}^2}{2m_e} - E_0\right]t - \frac{i}{m_e}\int_0^t dt'\left[e\boldsymbol{A}(t')\cdot\boldsymbol{p} - \frac{e^2\boldsymbol{A}^2(t')}{2}\right]\right\}. \tag{19}$$

Here, we have introduced the function $\tilde{\boldsymbol{\Phi}}(\boldsymbol{p})$, defined as

$$\tilde{\boldsymbol{\Phi}}(\boldsymbol{p}) = \int d^3r\,\boldsymbol{r}\Phi_0(\boldsymbol{r})e^{-i\boldsymbol{p}\cdot\boldsymbol{r}} = i\boldsymbol{\nabla}_{\boldsymbol{p}}\tilde{\Phi}_0(\boldsymbol{p}). \tag{20}$$

As before, $\tilde{\Phi}_0(\boldsymbol{p})$ denotes the Fourier transform of the bound-state wave function $\Phi_0(\boldsymbol{r})$, and $\boldsymbol{\nabla}_{\boldsymbol{p}}$ is the gradient calculated over momentum coordinates.

Once the amplitudes $\mathcal{A}^{V}(\boldsymbol{p})$ and $\mathcal{A}^{L}(\boldsymbol{p})$ are determined, we define the triply differential probability distribution of photodetachment $\mathcal{P}(\boldsymbol{p})$. According to the conventions adopted in this paper, we have

$$\mathcal{P}(\boldsymbol{p}) \equiv \frac{d^3P}{d^2\Omega_{\boldsymbol{p}}dE_{\boldsymbol{p}}} = \frac{m_e}{(2\pi)^3}|\boldsymbol{p}|\cdot|\mathcal{A}^{G}(\boldsymbol{p})|^2, \tag{21}$$

where $G = L, V$ is the gauge under consideration.

For our further purposes, we also introduce the differential probability $\bar{\mathcal{P}}(\boldsymbol{p})$,

$$\bar{\mathcal{P}}(\boldsymbol{p}) \equiv \frac{d^3P}{dp_xdp_ydp_z} = \frac{1}{(2\pi)^3}|\mathcal{A}^{G}(\boldsymbol{p})|^2, \tag{22}$$

for which the total probability of detachment P becomes

$$P = \int dp_xdp_ydp_z\bar{\mathcal{P}}(\boldsymbol{p}). \tag{23}$$

This expression will be useful for the Monte Carlo analysis presented in Sec. III C.

C. Wave function and its Fourier transform

To calculate the probability amplitudes $\mathcal{A}^{G}(\boldsymbol{p})$ of photodetachment, it is necessary to know the wave function of a weakly bound electron of a negative ion. Following [7,23], we rely on the asymptotic form of the respective wave function,

$$\Phi_0(\boldsymbol{r}) = \langle\boldsymbol{r}|\Phi_0\rangle \approx \frac{A}{r}e^{-\kappa r}Y_{\ell}^{m}(\theta_{\boldsymbol{r}}, \varphi_{\boldsymbol{r}}), \tag{24}$$

where A and $\kappa > 0$ are constant. Here, $Y_{\ell}^{m}(\theta_{\boldsymbol{r}}, \varphi_{\boldsymbol{r}})$ are the spherical harmonics, ℓ and m are the azimuthal and magnetic quantum numbers, respectively, and $\theta_{\boldsymbol{r}}$ and $\varphi_{\boldsymbol{r}}$ are the polar and azimuthal angles defining the position of the electron. The Fourier transform of the bound-state wave function (24) can be easily determined in spherical coordinates,

$$\begin{aligned}\tilde{\Phi}_0(\boldsymbol{p}) &= \int d^3r e^{-i\boldsymbol{p}\cdot\boldsymbol{r}}\Phi_0(\boldsymbol{r}) \\ &= A\int_0^{\infty} dr\int d^2\Omega_{\boldsymbol{r}}\, re^{-i\boldsymbol{p}\cdot\boldsymbol{r}}e^{-\kappa r}Y_{\ell}^{m}(\theta_{\boldsymbol{r}}, \varphi_{\boldsymbol{r}}).\end{aligned} \tag{25}$$

In order to calculate analytically the integrals in Eq. (25) we make use of the following plane wave decomposition [31]:

$$e^{i\boldsymbol{p}\cdot\boldsymbol{r}} = 4\pi\sum_{\ell'=0}^{\infty}\sum_{m'=-\ell'}^{\ell'} i^{\ell'}j_{\ell'}(pr)Y_{\ell'}^{m'*}(\theta_{\boldsymbol{p}}, \varphi_{\boldsymbol{p}})Y_{\ell'}^{m'}(\theta_{\boldsymbol{r}}, \varphi_{\boldsymbol{r}}), \tag{26}$$

where $j_{\ell'}(pr)$ are the spherical Bessel functions of the first kind. With the decomposition (26) we arrive at

$$\tilde{\Phi}_0(\boldsymbol{p}) = 4\pi A(-i)^{\ell} Y_{\ell}^{m}(\theta_{\boldsymbol{p}}, \varphi_{\boldsymbol{p}}) \int_0^{\infty} dr\, r\, j_{\ell}^{*}(pr) e^{-\kappa r}. \quad (27)$$

In the following, we shall focus only on the $1s$ orbital of H^-, meaning that $m = \ell = 0$ and $Y_0^0(\theta_{\boldsymbol{p}}, \varphi_{\boldsymbol{p}}) = 1/\sqrt{4\pi}$. In such a case the Fourier transform of the wave function (24) is given by

$$\tilde{\Phi}_{\mathrm{s}}(\boldsymbol{p}) = 2\sqrt{\pi} A \int_0^{\infty} dr \left(\frac{\sin pr}{p}\right) e^{-\kappa r}. \quad (28)$$

After performing the integral over r we obtain (see also Ref. [22])

$$\tilde{\Phi}_{\mathrm{s}}(\boldsymbol{p}) = \frac{2\sqrt{\pi} A}{\kappa^2 + \boldsymbol{p}^2}. \quad (29)$$

This formula depends only on the magnitude of momentum. Therefore, expression (20) can be easily calculated, leading to

$$\tilde{\boldsymbol{\Phi}}_{\mathrm{s}}(\boldsymbol{p}) = i\nabla_{\boldsymbol{p}} \tilde{\Phi}_{\mathrm{s}}(\boldsymbol{p}) = -i \frac{4\sqrt{\pi} A}{(\kappa^2 + \boldsymbol{p}^2)^2} \boldsymbol{p}. \quad (30)$$

The last two formulas will be used in (15) and (19) to calculate the probability amplitude of detachment of H^-. For this, we employ the values $A = 0.75$ a.u. and $\kappa = 0.2354$ a.u. from Ref. [23].

III. PHOTODETACHMENT BY ULTRASHORT LASER PULSES

We focus on photodetachment driven by an ultrashort laser pulse of circular polarization. In the dipole approximation, the electric field defining the pulse depends only on time through the phase $\phi = \omega t$. Here, $\omega = 2\pi/T_p$ represents the fundamental frequency of field oscillations. We shall also use the carrier frequency $\omega_{\mathrm{L}} = N_{\mathrm{osc}}\omega$, where N_{osc} is the number of cycles in a pulse. More specifically, we assume that the electric field is given by

$$\boldsymbol{\mathcal{E}}(\phi) = F_1(\phi)\boldsymbol{\varepsilon}_1 + F_2(\phi)\boldsymbol{\varepsilon}_2, \quad (31)$$

where the shape functions $F_j(\phi)$ are defined as

$$F_j(\phi) = F_0\, \omega \sin^2\left(\frac{\phi}{2}\right) \sin(N_{\mathrm{osc}}\phi + \delta_j) \cos(\delta + \delta_j) \quad (32)$$

for $\phi \in [0, 2\pi]$ and zero outside this interval. Here, F_0 is a constant prefactor which depends on the intensity of the field, and δ and δ_j determine its polarization properties. In particular, for circularly polarized pulses we choose $\delta_1 = 0$, $\delta_2 = \pi/2$, and $\delta = \pi/4$.

The vector potential corresponding to the laser pulse (31) $\boldsymbol{A}(\phi)$ is given by

$$\boldsymbol{A}(\phi) = f_1(\phi)\boldsymbol{\varepsilon}_1 + f_2(\phi)\boldsymbol{\varepsilon}_2, \quad (33)$$

with

$$f_j(\phi) = -\int_0^{\phi} d\phi' F_j(\phi'), \quad j = 1, 2. \quad (34)$$

With these definitions, we also guarantee that each function $f_j(\phi)$ vanishes at $\phi \leqslant 0$ and $\phi \geqslant 2\pi$. In the following, we assume that the polarization plane of the electromagnetic radiation is defined by the vectors $\boldsymbol{\varepsilon}_1 = \boldsymbol{e}_x$ and $\boldsymbol{\varepsilon}_2 = \boldsymbol{e}_y$ [see Eqs. (31) and (33)].

Even though the derivations presented above are rather general, our numerical calculations concern the photodetachment of the H^- ion ($|E_0| = 0.754$ eV) driven by a three-cycle ($N_{\mathrm{osc}} = 3$) CO_2 laser field ($\omega_{\mathrm{L}} = 0.117$ eV) or a THz field ($\omega_{\mathrm{L}} = 0.01$ eV) of circular polarization.

In Fig. 1 we present the temporal evolution of the tips of the vector potential $\boldsymbol{A}(\phi)$ (left panel) and electric field $\boldsymbol{\mathcal{E}}(\phi)$ (middle panel) for a CO_2 laser pulse of maximum intensity $I_{\max} = 5 \times 10^{11}$ W/cm^2 and frequency $\omega_{\mathrm{L}} = 0.117$ eV and comprising $N_{\mathrm{osc}} = 3$ oscillations within the $\sin^2$ envelope. The parametric plots start at the origin of coordinates and

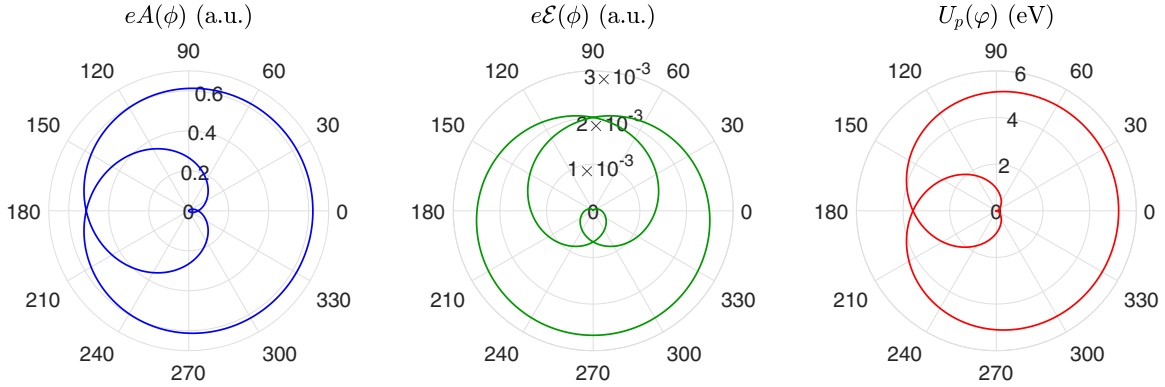

FIG. 1. Temporal evolution of the tips of the vector potential $\boldsymbol{A}(\phi)$ (left) and electric field $\boldsymbol{\mathcal{E}}(\phi)$ (middle), in atomic units, for the laser pulse (32). Both curves are plotted in the xy plane, and the angles are measured with respect to the positive $\boldsymbol{e}_x$ axis. Here, the carrier frequency corresponds to the CO_2 laser field ($\omega_{\mathrm{L}} = 0.117$ eV), the maximum intensity is $I_{\max} = 5 \times 10^{11}$ W/cm^2, and the pulse consists of three field oscillations within the $\sin^2$ envelope ($N_{\mathrm{osc}} = 3$). We have chosen the circular polarization for our calculations. The right panel shows a parametric plot of the instantaneous ponderomotive energy as a function of the azimuthal angle $U_p(\varphi)$ (see Sec. III A). All three curves start at the point (0,0) and evolve counterclockwise with the phase $\phi = \omega t$. For the THz laser pulse ($I_{\max} = 1 \times 10^{11}$ W/cm^2 and $\omega_{\mathrm{L}} = 0.01$ eV) we obtain curves with the exact same shape but multiplied by the scaling factors $r_A = 5.23$ (for the vector potential), $r_{\mathcal{E}} = 0.447$ (for the electric field), and $r_{U_p} = 27.38$ (for the ponderomotive energy).

evolve counterclockwise with increasing phase $\phi = \omega t$. The plots are generated in the xy-polarization plane. All angles are measured with respect to the positive $\boldsymbol{e}_x$ axis. In the right panel of Fig. 1 we also show the ponderomotive energy of the electron in the laser field, $U_p(\varphi) = e^2\boldsymbol{A}^2(\varphi)/(2m_e)$, for the same CO_2 laser pulse. The meaning and importance of such a curve will be discussed in Sec. III A. When the THz laser field is considered ($I_{\max} = 1 \times 10^{11}\,\mathrm{W/cm^2}$, $\omega_L = 0.01\,\mathrm{eV}$, and $N_{\mathrm{osc}} = 3$), we obtain parametric curves with the exact same shape but multiplied by the factors $r_A = 5.23$, $r_{\mathcal{E}} = 0.447$, and $r_{U_p} = 27.38$ for the vector potential, electric field, and ponderomotive energy, respectively.

A. Spiral of photodetachment

A fundamental requirement for the observation of EVSs is that the probability of photodetachment is large enough. Previously, in the case of photoionization, we showed that this happens only around well-defined regions in momentum space [27–29]. Such regions are determined by the so-called *spiral of ionization*, which arises from the saddle-point analysis of the probability amplitudes. This three-dimensional (3D) curve, which is parametrized by the phase of the laser field, defines the polar and azimuthal angles of detection and the magnitude of momentum for which electrons can be observed with highest probability. However, the spiral was originally defined for relativistic and quasirelativistic ionization processes, where the so-called *radiation pressure* plays an important role. In that case, the theory predicts that photoelectrons acquire an additional momentum in the direction of propagation of the laser field, hence the three-dimensional nature of the spiral. In contrast, in the current paper, photoelectrons are expected to appear near the polarization plane, which is due to the lack of electron recoil. Thus, the nonrelativistic momentum spiral is a flat, two-dimensional curve. Here, we define it without accounting for the radiation-pressure corrections (see Refs. [27–29]), i.e.,

$$\boldsymbol{p}_S(\phi) = e\boldsymbol{A}(\phi), \quad 0 \leqslant \phi \leqslant 2\pi. \tag{35}$$

As we have previously shown (see, e.g., Ref. [29]), the ponderomotive energy acquired by the electron in the light pulse at its time of birth (defined by a phase ϕ_0) is transformed into its asymptotic kinetic energy $E_{\boldsymbol{p}}$ after the interaction with the electromagnetic radiation is over. This observation remains valid both in the fully relativistic SFA (provided that the plane-wave-front approximation holds) and in classical physics. Let us consider an electron born at a time $t_0 = \phi_0/\omega$. It interacts with the electromagnetic field characterized by strength and direction of oscillations. While the latter can be defined by the azimuthal angle of emission $\varphi_{\boldsymbol{p}}$,

$$\varphi_{\boldsymbol{p}} = \arg[e\boldsymbol{A}(\phi_0)\cdot\boldsymbol{\varepsilon}_1 + ie\boldsymbol{A}(\phi_0)\cdot\boldsymbol{\varepsilon}_2], \tag{36}$$

the former is directly related to the instantaneous ponderomotive energy of the electron in the field,

$$U_p(\phi_0) = \frac{e^2\boldsymbol{A}^2(\phi_0)}{2m_e}, \tag{37}$$

which can be rewritten as

$$U_p(\phi_0) = \frac{[\boldsymbol{p}_S(\phi_0)]^2}{2m_e}. \tag{38}$$

According to our previous investigations [27–29,32], this quantity determines the asymptotic kinetic energy of the photoelectron after the interaction with the short laser pulse is over, i.e., $E_{\boldsymbol{p}} = U_p(\phi_0)$. In other words, by drawing the ponderomotive energy as a function of φ while it is parametrized by the phase of the light pulse ϕ, we have access to information concerning the final energy of the electron and its direction of emission. We will call such a curve the *ponderomotive spiral* $U_p(\varphi)$. It is shown in the right panel of Fig. 1 for the laser field parameters $I_{\max} = 5 \times 10^{11}\,\mathrm{W/cm^2}$, $\omega_L = 0.117\,\mathrm{eV}$.

The ponderomotive spiral of ionization (or its extrapolation to photodetachment) driven by ultrashort laser pulses has many applications. For instance, given any azimuthal angle of detection $\varphi_{\boldsymbol{p}}$, the curve $U_p(\varphi_{\boldsymbol{p}})$ determines the energies at which photoelectrons can be detected with significant probabilities. Furthermore, the self-crossings of the spiral define regions in space where intense interference effects can be observed [27–29,32]. Note, however, that there are certain restrictions to its predictions; the results arising from the spiral are accurate provided that the energy of photoelectrons is around or larger than ten times the ionization potential of the target ($E_{\boldsymbol{p}} \gtrsim 10|E_0|$), independent of whether the binding potential is of Coulomb type or ZRP. If this condition is not fulfilled, the spiral describes the angular-resolved energy spectra of photoelectrons only qualitatively. The equation defining the spiral is obtained by approximating the complex saddle points, which contribute substantially to the probability amplitude of ionization, by their real values. This implies that the dominant saddle points must be characterized by small imaginary parts. As we showed in Refs. [27–29,32], this is exactly the case when the condition $E_{\boldsymbol{p}} \gtrsim 10|E_0|$ applies.

B. Energy spectra of electrons in photodetachment

Here we shall analyze probability distributions of photoelectrons detached from the H^- ion by the ultrashort laser pulse described in Sec. III. In Fig. 2, the triply differential probability distributions $\mathcal{P}(\boldsymbol{p})$ [Eq. (21)] are plotted as functions of the electron kinetic energy $E_{\boldsymbol{p}} = \boldsymbol{p}^2/(2m_e)$. Those distributions are calculated for the polar angle of detection $\theta_{\boldsymbol{p}} = \pi/2$ and the azimuthal angle $\varphi_{\boldsymbol{p}} = 0$, i.e., along the $\boldsymbol{e}_x$ axis. The top panel corresponds to the photodetachment driven by the CO_2 laser field ($I_{\max} = 5 \times 10^{11}\,\mathrm{W/cm^2}$ with $\omega_L = 0.117\,\mathrm{eV}$), and we show the results in the velocity (dotted red line) and length (solid blue line) gauges. Both gauges give identical results for the $1s$ bound state of the ZRP. Such a result is far from obvious since the analytical formulas defining the probability amplitudes differ considerably [see Eqs. (15) and (19)]. Interestingly, the numerical calculation involving the velocity gauge are more demanding from the computational point of view, as the integrand in Eq. (15) oscillates with a larger amplitude. Note that, in Ref. [23], Gribakin and Kuchiev already mentioned the gauge invariance of the probability distributions when the unperturbed atomic anion is found in the $1s$ state of the ZRP. Hence, we corroborate that the results obtained from velocity and length gauges are, in fact, identical for photodetachment from such a state. In the bottom panel of Fig. 2 we show the energy spectra of electrons $\mathcal{P}(\boldsymbol{p})$ [Eq. (21)], driven by the THz laser field described above

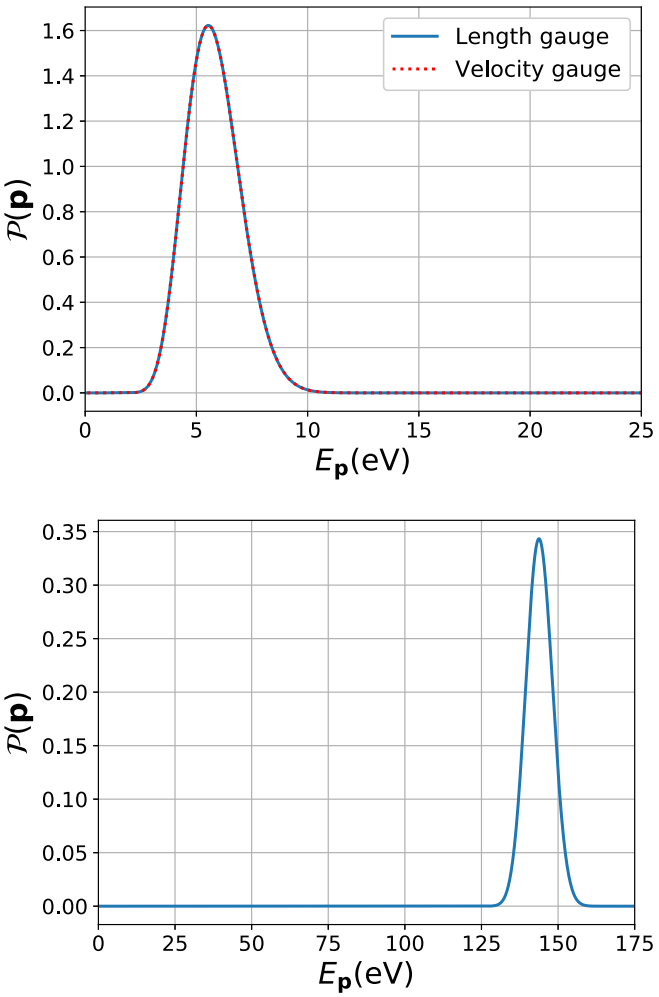

FIG. 2. Probability distribution (in atomic units) of electron photodetachment $\mathcal{P}(\boldsymbol{p})$ [Eq. (21)] from the H^- ion ($1s$ state of the ZRP) as a function of the electron kinetic energy $E_{\boldsymbol{p}} = \boldsymbol{p}^2/(2m_e)$. The driving field is a three-cycle, circularly polarized laser pulse, as described in Sec. III. The polar and azimuthal angles of electron detection are $\theta_{\boldsymbol{p}} = \pi/2$ and $\varphi_{\boldsymbol{p}} = 0$, respectively; that is, electrons are detected along the $\boldsymbol{e}_x$ axis. In the top panel we show the energy distribution for the laser field intensity $I_{\max} = 5 \times 10^{11}\,\mathrm{W/cm^2}$ and frequency $\omega_L = 0.117\,\mathrm{eV}$, in the length (solid blue line) and velocity (dotted red line) gauges. In the bottom panel we present the same but for a driving field of intensity $I_{\max} = 1 \times 10^{11}\,\mathrm{W/cm^2}$ and frequency $\omega_L = 0.01\,\mathrm{eV}$. In this panel, only the results corresponding to the length gauge are shown (see the text).

($I_{\max} = 1 \times 10^{11}\,\mathrm{W/cm^2}$ with $\omega_L = 0.01\,\mathrm{eV}$). This time we present only the results obtained in the length gauge since, as we have checked, the velocity gauge leads to the exact same curve, with a larger computational effort.

The probability distributions shown in the top and bottom panels of Fig. 2 are very small except around well-defined photoelectron energies. There, pronounced lobes which span along tens (or hundreds, for the THz pulse) of single-photon energies appear without signs of multiphoton interference effects (peaks). Similar interference-free structures have been theoretically predicted in relativistic photoionization driven by ultrashort laser pulses and are known as *supercontinua* [32–34].

Now, let us analyze the relation between the ponderomotive spiral of ionization $U_p(\varphi) = [\boldsymbol{p}_S(\varphi)]^2/(2m_e)$ (right panel of Fig. 1) and the spectra of photoelectrons presented in Fig. 2. For a laser field of intensity $I_{\max} = 5 \times 10^{11}\,\mathrm{W/cm^2}$ and frequency $\omega_L = 0.117\,\mathrm{eV}$ and at polar and azimuthal angles of detection $\theta_{\boldsymbol{p}} = \pi/2$ and $\varphi_{\boldsymbol{p}} = 0$, the spiral predicts the formation of a large interference-free structure located at energies around $E_{\boldsymbol{p}} = 5.24\,\mathrm{eV}$. This can be seen by looking at the values at $U_p(\varphi = 0)$ (right panel of Fig. 1). In the top panel of Fig. 2 we see that the supercontinuum acquires its actual maximum at $E_{\boldsymbol{p}} \approx 5.5\,\mathrm{eV}$. For this photoelectron energy, the spiral describes only qualitatively the photodetachment process, as $E_{\boldsymbol{p}} < 7.54\,\mathrm{eV} = 10|E_0|$. Nevertheless, the maximum probability is achieved close to the predicted 5.24 eV.

For the smaller intensity $I_{\max} = 1 \times 10^{11}\,\mathrm{W/cm^2}$ and frequency $\omega_L = 0.01\,\mathrm{eV}$, the curve $U_p(\varphi = 0)$ predicts the formation of a supercontinuum at $E_{\boldsymbol{p}} \approx 143.5\,\mathrm{eV}$ (see the right panel of Fig. 1 accounting for the multiplicative factor $r_{U_p} = 27.38$). The actual maximum is found at around $E_{\boldsymbol{p}} \approx 143.7\,\mathrm{eV}$ (bottom panel of Fig. 2), which is very close to the expected value.

With those observations we conclude that, similar to the 3D spiral in the relativistic (or quasirelativistic) SFA [5,6,27–29], the two-dimensional ponderomotive spiral in nonrelativistic photodetachment predicts the energy regions for which the angle-resolved spectra of photoelectrons show significant probabilities. Furthermore, for the photodetachment from the $1s$ state of the H^- ion, both velocity and length gauges lead to the exact same probability distributions, even though the analytical expressions for the amplitudes are substantially different.

Up to now we have shown how the ionization spiral determines the position of maximum probability in the energy spectra of photoelectrons. In light of the synthesis of ultrashort electron wave packets [28,32–35], it is important, however, to discuss the width of the supercontinuum as well. In general, for a given laser carrier frequency, larger field intensities lead to broader supercontinua, as demonstrated in Refs. [28,32,35]. On the other hand, by comparing the top and bottom panels of Fig. 2, we see that the frequency of the laser pulse also affects the width of supercontinua; by decreasing the intensity by a factor of 5 (from 5×10^{11} to $1 \times 10^{11}\,\mathrm{W/cm^2}$) and reducing the frequency by a factor of 10 (from $\omega_L = 0.117\,\mathrm{eV}$ to $\omega_L = 0.01\,\mathrm{eV}$), the full width at half maximum of the supercontinuum increases from 2.8 eV up to 10 eV. Hence, one could conclude that smaller frequencies and higher intensities produce broader structures in the energy spectra of photoelectrons. Furthermore, the relative width of the supercontinuum structure, i.e., the ratio of the width to the central energy, becomes smaller. In general, numerical analysis shows that although the supercontinuum central energy increases together with the temporal ponderomotive energy, its relative width becomes more narrow. This indicates that the concept of the ionization spiral is particularly well suited to describe the high-energy ionization spectrum.

C. Coarse-grained probability distributions and total probabilities

In this section, we shall calculate the CGPDs using the Monte Carlo method. This is done in a way similar to what we presented in Ref. [36]. To this end, we assume that the differential probability distribution $\bar{\mathcal{P}}(\boldsymbol{p})$ [Eq. (22)] is negligibly small outside the rectangular cuboid in momentum space defined by the parameters $p_a^{\min} \leqslant p_a \leqslant p_a^{\max}$, where $a = x, y$ or z. To perform the Monte Carlo integration, we introduce three variables $\boldsymbol{\xi} \equiv (\xi_x, \xi_y, \xi_z)$ such that $\xi_a \in [0, 1]$. It is possible to map this unit cube in $\boldsymbol{\xi}$ into the whole integration box by means of the transformation

$$p_a = p_a^{\min} + \xi_a\big(p_a^{\max} - p_a^{\min}\big). \tag{39}$$

For simplicity, we define the vectors $\boldsymbol{p}^{\min} \equiv (p_x^{\min}, p_y^{\min}, p_z^{\min})$ and $\boldsymbol{p}^{\max} \equiv (p_x^{\max}, p_y^{\max}, p_z^{\max})$. The total probability of photodetachment is then obtained as

$$P = \int_0^1 d^3\xi\, \bar{\mathcal{P}}(\boldsymbol{\xi}). \tag{40}$$

Here, the function $\bar{\mathcal{P}}(\boldsymbol{\xi})$ is given by

$$\bar{\mathcal{P}}(\boldsymbol{\xi}) = \left|\frac{\partial \boldsymbol{p}}{\partial \boldsymbol{\xi}}\right| \bar{\mathcal{P}}(\boldsymbol{p}(\boldsymbol{\xi})), \tag{41}$$

$\bar{\mathcal{P}}(\boldsymbol{p})$ is defined in Eq. (22), and

$$\left|\frac{\partial \boldsymbol{p}}{\partial \boldsymbol{\xi}}\right| = \big(p_x^{\max} - p_x^{\min}\big)\big(p_y^{\max} - p_y^{\min}\big)\big(p_z^{\max} - p_z^{\min}\big) \tag{42}$$

is the Jacobian of the transformation.

To obtain the coarse-grained probability distribution, we divide the unit cube in $\boldsymbol{\xi}$ into 2^{3n} subcubes of constant volume $(\Delta\xi)^3 = 2^{-3n}$ (in the numerical analysis presented below, $n = 10$). Each one of them can be identified by the three integers $i, j, k \in [1, 2^n]$. Such discretization allows us to define a set of continuous variables ξ_x^i, ξ_y^j, and ξ_z^k that run along the edges of the (i, j, k) subcube. Namely,

$$(\alpha - 1)2^{-n} \leqslant \xi_a^\alpha < \alpha 2^{-n}, \quad \alpha = 1, 2, \ldots, (2^n - 1), 2^n, \tag{43}$$

with $\alpha = i, j, k$. It follows from these definitions that $\xi_a^{\alpha+1} = \xi_a^\alpha + \Delta\xi$. The CGPD is then obtained by integrating the differential distribution (41) over all intervals in one ξ coordinate and over the remaining two-dimensional (2D) rectangle of area $(\Delta\xi)^2$ (i.e., it is the probability distribution projected onto a two-dimensional surface). For instance, the coarse-grained probability distribution in the $\xi_a\xi_b$ plane $\bar{\mathcal{P}}_{\alpha,\beta}^{(\xi_a,\xi_b)}$ reads (we use the simplified notation $a, b, c = x, y, z$ and $\alpha, \beta = i, j, k$)

$$\bar{\mathcal{P}}_{\alpha,\beta}^{(\xi_a,\xi_b)} = \int_{\xi_a^\alpha}^{\xi_a^\alpha + \Delta\xi} d\xi_a \int_{\xi_b^\beta}^{\xi_b^\beta + \Delta\xi} d\xi_b \int_0^1 d\xi_c \bar{\mathcal{P}}(\boldsymbol{\xi}), \tag{44}$$

where $\bar{\mathcal{P}}(\boldsymbol{\xi})$ is given in (41). In this way we obtain the projections onto three planes: $(\xi_x\xi_y)$, $(\xi_x\xi_z)$, and $(\xi_y\xi_z)$. In our numerical illustrations, we scale the total probability (sum over all grains) to 1.

With the construction described above, the CGPD becomes a two-dimensional distribution of the integrated probability. The size of each "grain" or "pixel" is determined by the number of intervals 2^n, as $(\Delta\xi)^2 = 2^{-2n}$. However, in real experiments, even high-resolution detectors can provide only an average count of electrons within a momentum interval. For this reason, it is useful to introduce a two-dimensional Gaussian window $W(\xi_a, \xi_b)$ to obtain the average of the probability distribution in the $\xi_a\xi_b$ plane $\bar{\mathcal{P}}_W(\xi_a, \xi_b)$,

$$\bar{\mathcal{P}}_W(\xi_a, \xi_b) = \int_0^1 d^3\zeta\; W(\xi_a - \zeta_a, \xi_b - \zeta_b)\bar{\mathcal{P}}(\boldsymbol{\zeta}), \tag{45}$$

where the integration is carried out over $\boldsymbol{\zeta} = (\zeta_x, \zeta_y, \zeta_z)$ and $\bar{\mathcal{P}}(\boldsymbol{\zeta})$ is given in Eq. (41). Like for the case of the CGPD, we obtain a two-dimensional projection of the averaged probability distribution onto the $\xi_x\xi_y$, $\xi_x\xi_z$, and $\xi_y\xi_z$ planes, and the total probability is scaled to 1. In our calculations, we have chosen a Gaussian function multiplied by another smoothly varying function which vanishes at $\xi_a, \xi_b = -1/2, 1/2$. In particular, we use

$$W(\xi_a, \xi_b) = \frac{1}{4}(1 + \cos 2\pi\xi_a)(1 + \cos 2\pi\xi_b) \times \exp\left[-\frac{\xi_a^2 + \xi_b^2}{\sigma^2}\right], \tag{46}$$

with $\sigma = 0.1$.

In the left column of Fig. 3 we present the color mapping of the CGPDs $[\bar{\mathcal{P}}_{\alpha,\beta}^{(\xi_a,\xi_b)}]^r$ [Eq. (44)] calculated with respect to $\xi_x\xi_y$ (top panel), $\xi_x\xi_z$ (middle panel), and $\xi_y\xi_z$ (bottom panel) for the laser pulse described in Fig. 1. To highlight the main features of the distribution, we elevate the CGPD to the power $r = 0.5$. In the right column we show the same, but for the averaged probability $\bar{\mathcal{P}}_W(\xi_a, \xi_b)$. The difference between those two calculations is that the averaged distribution enhances the features of the projected ATD probabilities, so it can be compared with potential experimental results. To obtain those figures we have set the integration box in momentum space as defined by the parameters $\boldsymbol{p}^{\max} = (1.5, 1.5, 0.3)$ (in atomic units) and $\boldsymbol{p}^{\min} = -\boldsymbol{p}^{\max}$. The Monte Carlo integration was performed with 2.4×10^6 points and with a standard deviation smaller than 2%. From the top row of Fig. 3 we see that, in the $\xi_x\xi_y$ plane, the coarse-grained (and averaged) probability distribution achieves high values in regions which coincide with the outer ring of the 2D spiral. The latter, for the same parameters, is plotted in $\boldsymbol{\xi}$ space in the top panel of Fig. 4. This is expected, as the photodetachment is more probable at large field strengths, i.e., when $U_p(\varphi)$ is large. Moreover, the actual maximum is found at the phase $\phi = \pi$, i.e., when the time-dependent ponderomotive energy of the electron in the laser field is peaked. From the middle and bottom rows we see that the photodetachment happens close to the $\xi_x\xi_y$ plane, which is a consequence of the flatness of the detachment spiral (note also that the parameters defining the transformation into $\boldsymbol{\xi}$ space are $p_x^{\max} = p_y^{\max} > p_z^{\max}$). In contrast, when radiation pressure is taken into account (relativistic or quasirelativistic SFA calculations), the equivalent 3D curve circulates over the surface of an elliptic paraboloid with the axis at $\xi_x = \xi_y = 0.5$ (see Ref. [36]).

The total probability of photodetachment (40) is calculated by Monte Carlo methods as a function of the number of field oscillations $N_{\rm osc}$. The remaining parameters of the laser field are the same as in Fig. 1 (intensity $I_{\max} = 5 \times 10^{11}\,\mathrm{W/cm^2}$ and frequency $\omega_{\rm L} = 0.117\,\mathrm{eV}$). The results are shown in

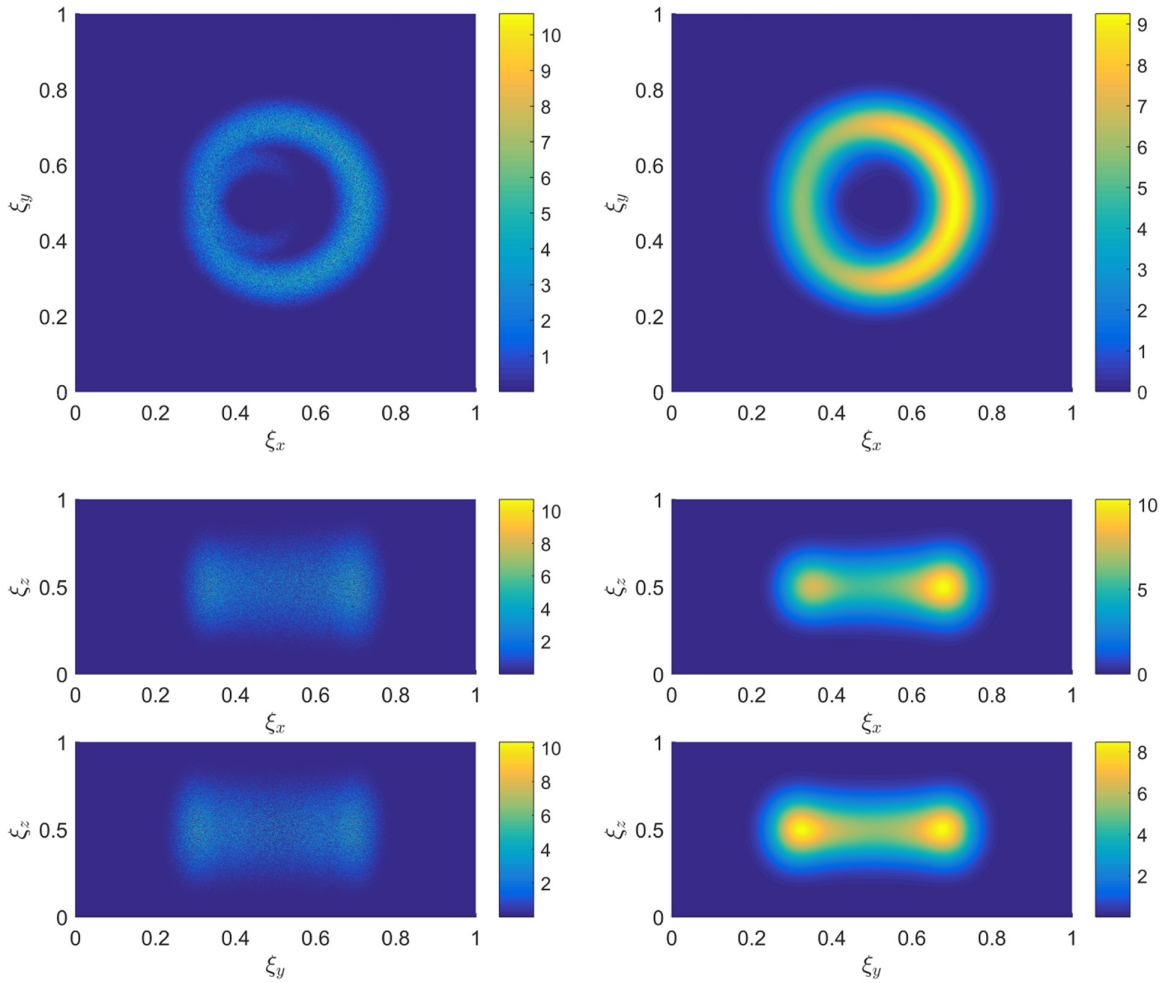

FIG. 3. Dimensionless and scaled [see the text below Eq. (44)] coarse-grained probability distributions $[\bar{\mathcal{P}}^{(\xi_a,\xi_b)}_{\alpha,\beta}]^{0.5}$ [Eq. (44) raised to the power 0.5 for visual purposes; left column] and averaged and scaled [see the text below Eq. (45)] probability distributions $\bar{\mathcal{P}}_W(\xi_a,\xi_b)$ (right column) of photoelectrons detached from the H^- ion. The laser field is as described in Fig. 1 ($I_{\max} = 5\times10^{11}\,\mathrm{W/cm^2}$ and $\omega_L = 0.117\,\mathrm{eV}$). While the top row corresponds to the projection onto the $\xi_x\xi_y$ plane, the middle and bottom rows are the projections onto the $\xi_x\xi_z$ and $\xi_y\xi_z$ planes, respectively. These photoelectron momentum correlations show that the detachment taking place in the polarization (xy) plane is dominated by momenta in the vicinity of the outer rings of the 2D spiral of ionization. We observe that detachment probabilities for small energies are negligible. In order to restore the absolute values, the scaled distributions $\bar{\mathcal{P}}^{(\xi_a,\xi_b)}_{\alpha,\beta}$ and $\bar{\mathcal{P}}_W(\xi_a,\xi_b)$ should be multiplied by the total probability equal to 0.25.

Fig. 5. One can see that the total probability P increases linearly with the number of cycles, and it is always less than unity for the driving field considered here. Under those circumstances it becomes meaningful to introduce the concept of detachment rates $\mathcal{W}$, even if the driving fields are of ultrashort (few-cycle) duration. From Fig. 5 we estimate that the photodetachment rate, defined as

$$\mathcal{W} = \frac{P(N_{\mathrm{osc}})}{2\pi N_{\mathrm{osc}}/\omega_L}, \tag{47}$$

is $\mathcal{W} \approx 2.3\times10^{12}\ \mathrm{s}^{-1}$. Note, however, that the theoretical approach used in this paper is valid for moderate-field intensities, such that the depletion of the ground state within one cycle is much smaller than 1. Driving fields with $I_{\max} > 5\times10^{12}\,\mathrm{W/cm^2}$ could lead to unphysical probabilities exceeding unity even for a three-cycle pulse. For this reason, we restrict our calculations to fields of maximum intensity $I_{\max} = 5\times10^{11}\,\mathrm{W/cm^2}$ or lower, such that the total probabilities of detachment within one cycle are sufficiently small. In such a case and by making use of the detachment rates (47), we can redefine the probability of photodetachment accounting for depletion effects, i.e.,

$$P = 1 - \exp\left(-2\pi\frac{\mathcal{W}N_{\mathrm{osc}}}{\omega_L}\right). \tag{48}$$

For the case when $\mathcal{W} \ll \omega_L/(2\pi)$, we obtain again the relation $P \approx \mathcal{W}(2\pi N_{\mathrm{osc}}/\omega_L)$.

In Fig. 6 we present the same information as in Fig. 3, but for the THz laser field ($I_{\max} = 1\times10^{11}\,\mathrm{W/cm^2}$ and $\omega_L = 0.01\,\mathrm{eV}$). The CGPD is elevated to the power $r = 0.2$. This time, the integration box in momentum space is defined by the vectors $\boldsymbol{p}^{\max} = (4.5, 4.5, 0.4)$ (in atomic units) and $\boldsymbol{p}^{\min} = -\boldsymbol{p}^{\max}$. Here, 2.4×10^6 points are used in the Monte Carlo integration, ensuring the convergence of the results. The standard deviation does not exceed 4%. As can be seen, the probability distribution projected onto the $\xi_x\xi_y$ plane (coarse

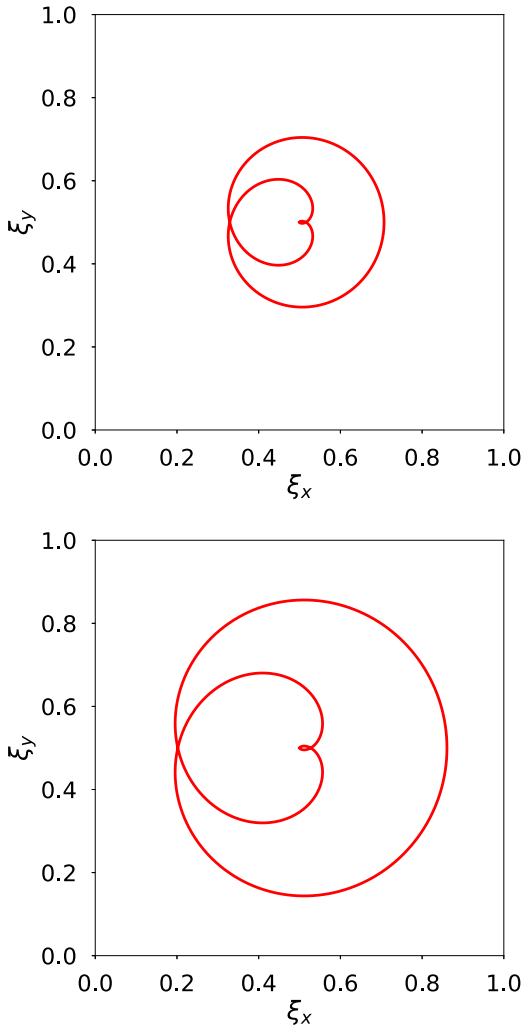

FIG. 4. Spirals of photodetachment $\boldsymbol{p}_S(\phi)$ [Eq. (35)] in $\boldsymbol{\xi}$ space. The transformation is performed according to Eq. (39). The top panel corresponds to the laser field shown in Fig. 1 with the parameters $\boldsymbol{p}^{\max} = (1.5, 1.5, 0.3)$ and $\boldsymbol{p}^{\min} = -\boldsymbol{p}^{\max}$, in atomic units. The bottom panel refers to the THz laser pulse with $\boldsymbol{p}^{\max} = (4.5, 4.5, 0.4)$ a.u. and $\boldsymbol{p}^{\min} = -\boldsymbol{p}^{\max}$. The outer rings of the spirals determine the momenta for which detachment takes place with dominant probabilities (see Figs. 3 and 6).

grained or averaged) also follows the outer ring of the spiral (compare with the bottom panel in Fig. 4) with maximum values near the phase $\phi = \pi$. The $\xi_x\xi_z$ and $\xi_y\xi_z$ projections also indicate that the photodetachment occurs close to the $\xi_x\xi_y$ plane.

As for the case of the CO_2 pulse (see Fig. 5), the total probability of electron detachment for THz pulses increases linearly with the number of cycles $N_{\rm osc}$ in the pulse. Our Monte Carlo estimations show that the total photodetachment probability per cycle is $P/N_{\rm osc} \approx 0.006$, which gives the rate $\mathcal{W} \approx 1.5 \times 10^{10}\ \mathrm{s}^{-1}$ for the considered peak intensity.

To summarize this section, we have analyzed the CGPDs as opposed to doubly differential probability distributions of photodetachment [i.e., $\bar{\mathcal{P}}(\boldsymbol{p})$ integrated over one momentum coordinate] to relate to finite resolution in a measurement of electron momenta. Note that measuring instruments detect

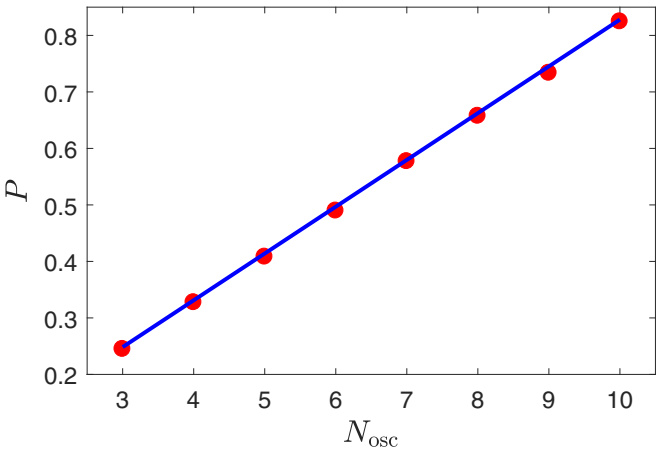

FIG. 5. Total probability of electron detachment P [Eq. (40)] as a function of the number of field oscillations $N_{\rm osc}$. The driving field is circularly polarized with a maximum intensity $I_{\max} = 5 \times 10^{11}\,\mathrm{W/cm^2}$ and frequency $\omega_L = 0.117\,\mathrm{eV}$ (CO_2 laser field). The total number of points used for the integration is not less than 10^6, until convergence is ensured, and the resulting standard deviation is smaller than 2%.

electrons only within a certain range of momentum $\Delta|\boldsymbol{p}|$ and angles. For instance, in a standard velocity map imaging spectroscopy the ratio $\Delta|\boldsymbol{p}|/|\boldsymbol{p}|$ is around 1% [36,37]. Hence, the resolution of momentum measurement can be related to the size of pixels in two-dimensional density plots shown in the left panels of Figs. 3 and 6. If the experimental setup is such that the electron count is averaged not only over $\Delta|\boldsymbol{p}|$ but also over angles, then the CGPDs shown in the right panels will describe the measured data. Finally, note that the two-dimensional probability distribution obtained by integrating without the Gaussian window would lead to similar patterns, but with subtle interference structures (see, e.g., [27]) that can hardly be resolved in an experiment.

IV. ELECTRON VORTEX STATES IN PHOTODETACHMENT

In order to obtain EVSs, it is necessary that the asymptotic momentum of the photoelectron $\boldsymbol{p}$ circulates along the surface of a cone with a well-defined symmetry axis [5,6]. According to the analysis presented in Sec. III A, if such a cone approaches the spiral of ionization in momentum space, EVSs with substantial topological charge can be detected with significant probability. We start by defining the cone's symmetry axis as the unit vector $\boldsymbol{n}_\parallel$ (pointing at the polar and azimuthal angles θ_T and φ_T, measured with respect to the xz plane). It can be used to establish a set of three orthonormal vectors in momentum space, denoted as $\boldsymbol{n}_\parallel$, $\boldsymbol{n}_{\perp,1}$, and $\boldsymbol{n}_{\perp,2}$, such that $\boldsymbol{n}_\parallel = \boldsymbol{n}_{\perp,1} \times \boldsymbol{n}_{\perp,2}$ (see Refs. [5,6]). In this system of coordinates, the circulating momentum $\boldsymbol{p}_T$ can be parametrized by the so-called *twist angle* φ in the following way:

$$\boldsymbol{p}_T(\varphi) = p_T \sin\beta_T(\boldsymbol{n}_{\perp,1}\cos\varphi + \zeta_H \boldsymbol{n}_{\perp,2}\sin\varphi) + p_T\cos\beta_T \boldsymbol{n}_\parallel. \quad (49)$$

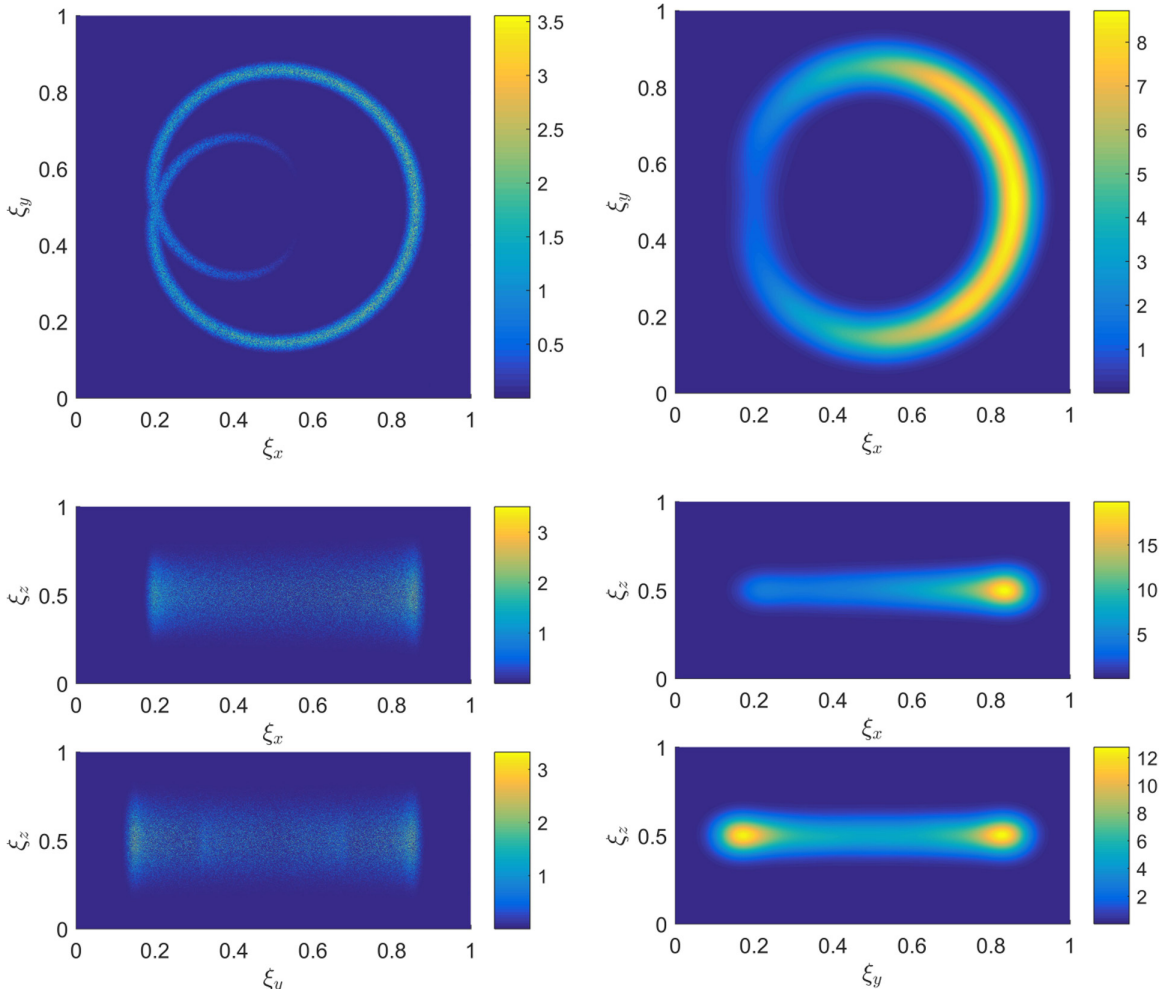

FIG. 6. The same as in Fig. 3, but for the THz laser field ($I_{\max} = 1 \times 10^{11}\,\mathrm{W/cm^2}$ and $\omega_L = 0.01\,\mathrm{eV}$). To highlight the main features of the distribution, the CGPD is presented as $[\bar{\mathcal{P}}^{(\xi_a,\xi_b)}_{\alpha,\beta}]^{0.2}$. By doing so we also observe, at least partially, the inner part of the ionization spiral. The absolute values of the scaled distributions $\bar{\mathcal{P}}^{(\xi_a,\xi_b)}_{\alpha,\beta}$ and $\bar{\mathcal{P}}_W(\xi_a,\xi_b)$ are restored by multiplying them by the total probability, which is equal to 0.018.

Here, $2\beta_T$ and p_T are the opening angle and slant length of the cone, respectively, and $\zeta_H = \pm 1$ determines the direction of circulation. For our calculations we set $\zeta_H = 1$. A superposition of electron states with momentum (49) over all twist angles ($0 \leqslant \varphi < 2\pi$) carries nonzero angular momentum (provided that $\beta_T \neq 0$); that is, it corresponds to a propagating EVS. As our goal is the analysis of such vortex states in photodetachment, we start by determining the probability amplitude for the transition from the bound state to a twisted state. Namely, we want to calculate $\mathcal{A}(\boldsymbol{p}_T(\varphi))$ in the length and velocity gauges. It is convenient to perform a base transformation from the plane-wave states $|\boldsymbol{p}\rangle$ to the so-called Bessel states $|p_\parallel, p_\perp, M\rangle$ (see, e.g., Refs. [5,6]). Here, the labels $p_\parallel$ and $p_\perp$ correspond to the parallel and perpendicular components of momentum with respect to the cone's symmetry axis, i.e.,

$$p_\parallel = \boldsymbol{p}\cdot\boldsymbol{n}_\parallel, \quad p_\perp = \sqrt{\boldsymbol{p}^2 - p_\parallel^2}, \tag{50}$$

and M is the topological charge. In position representation, the Bessel states are given by [5,6]

$$\langle \boldsymbol{r}|p_\parallel, p_\perp, M\rangle = i^M e^{ip_\parallel r_\parallel} J_M(p_\perp x_\perp) e^{iM\varphi_r}, \tag{51}$$

where $J_M(p_\perp x_\perp)$ are the Bessel functions of the first kind. The probability amplitude of photodetachment into the Bessel state with topological charge M is [5]

$$\mathcal{A}^G(p_\parallel, p_\perp, M) = \frac{1}{2\pi}\int_0^{2\pi} d\varphi e^{-iM\varphi}\mathcal{A}^G(\boldsymbol{p}_T(\varphi)), \tag{52}$$

where $G = L, V$ stands for the chosen gauge. By means of (52) we can obtain the probability amplitude of detachment into *field-free* vortex states. Note that our analysis concerns photodetachment by short laser pulses in the dipole approximation. This means that, after a time T_p, the photoelectron does not interact anymore with the light field. If that was not the case (for instance, when an infinite plane wave acts upon the negative ion), the final state would have to be modeled as a laser-modified Bessel state (see, e.g., [38]). However, this type of treatment, independent of the fact that its validity can

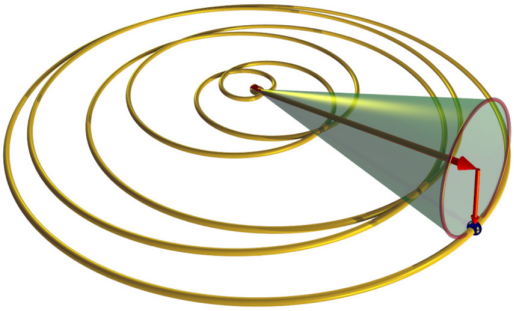

FIG. 7. Schematic representation of the two-dimensional spiral of ionization $\boldsymbol{p}_S(\phi)$ (solid yellow curve) and the cone of circulating momentum $\boldsymbol{p}_T(\varphi)$ (semitransparent green surface) for the geometry considered in this paper (note that, for visual purposes, the diagram represents the case of a laser field containing seven oscillations, $N_{osc} = 7$). If β_T is the half-opening angle, the cone's symmetry axis $\boldsymbol{n}_\parallel$ is chosen such that $\theta_T = \frac{\pi}{2} - \beta_T$ (thick red arrow). The thin vertical arrow points along the direction of the vector $\boldsymbol{n}_{\perp,1}$ in Eq. (49). For the parameters used here (see text), the twisted momentum $\boldsymbol{p}_T(\varphi)$ touches the spiral at $\phi_0 = \pi$ and $\varphi_0 = 0$.

be questioned for few-cycle pulses, is beyond the scope of the present paper.

To obtain high topological charge EVSs we build the cone of circulating momenta $\boldsymbol{p}_T(\varphi)$ [Eq. (49)] in such a way that it touches the spiral $\boldsymbol{p}_S(\phi)$ [Eq. (35)] at a given phase ϕ_0 and twist angle φ_0. In particular, we choose $\phi_0 = \pi$ (middle of the pulse). For this particular value and for the laser fields considered here, the ponderomotive spiral predicts large probabilities of electron detection at the azimuthal angle $\varphi_{\boldsymbol{p}} = 0$ (see the right panel in Fig. 1). Hence, by setting the symmetry axis of the cone [$\boldsymbol{n}_\parallel$ in Eq. (49)] pointing at a polar angle $\theta_T = \frac{\pi}{2} - \beta_T$ and azimuthal angle $\varphi_T = 0$, we guarantee that the twisted momentum touches the spiral at $\varphi_0 = 0$. The magnitude p_T is chosen such that $|\boldsymbol{p}_T(\varphi_0)| = |\boldsymbol{p}_S(\phi_0)|$. This geometry is illustrated in Fig. 7 for $N_{osc} = 7$.

A. OAM distributions in photodetachment

Now, we proceed with calculations of the probability distribution of detachment $\mathcal{P}(\boldsymbol{p}_T(\varphi))$ [see Eqs. (21) and (49)] and the corresponding OAM distribution, defined as $|\mathcal{A}(p_\parallel, p_\perp, M)|^2$ [see Eq. (52)]. This is done according to the construction prescribed above, which is based on the concept of the spiral. For our further calculations, we choose the touching phase $\phi_0 = \pi$ and the cone's opening half-angle $\beta_T = 0.1\pi$. Under those conditions, its symmetry axis is defined by the angles $\theta_T = 0.4\pi$ and $\varphi_T = 0$. The magnitude of the twisted momentum p_T is chosen such that the cone abuts the spiral at $\varphi_T = 0$ (modulo 2π).

In Fig. 8 we show the probability distribution as a function of the twist angle $\mathcal{P}(\varphi) \equiv \mathcal{P}(\boldsymbol{p}_T(\varphi))$ (top panel) and the OAM distribution $|\mathcal{A}(p_\parallel, p_\perp, M)|^2$ (bottom panel) for the photodetachment from the $1s$ state of the H^- ion. Both curves are scaled to their maximum values. The laser field is as described in Fig. 1; that is, its maximum intensity is $I_{max} = 5 \times 10^{11}\,\mathrm{W/cm^2}$ and its carrier frequency is $\omega_L = 0.117\,\mathrm{eV}$. The parallel and perpendicular components of the twisted momentum [see, Eq. (50)] are chosen such that

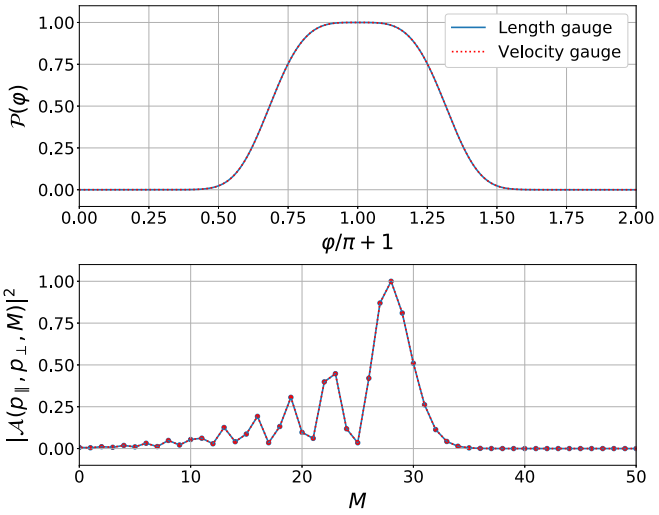

FIG. 8. The top panel shows the probability distribution of photodetachment $\mathcal{P}(\boldsymbol{p}_T(\varphi))$ as a function of the twist angle φ. In the bottom panel we present the corresponding OAM distribution $|\mathcal{A}(p_\parallel, p_\perp, M)|^2$. Both quantities are scaled to their maximum values. The geometry in momentum space is described in the text, with the half-opening angle $\beta_T = 0.1\pi$ and the cone's symmetry axis defined by the polar and azimuthal angles $\theta_T = 0.4\pi$ and $\varphi_T = 0$, respectively. The driving field is shown in Fig. 1 with a maximum intensity $I_{max} = 5 \times 10^{11}\,\mathrm{W/cm^2}$ and carrier frequency $\omega_L = 0.117\,\mathrm{eV}$. For the OAM distribution, the parallel and perpendicular components of momentum are $p_\parallel = 0.59$ a.u. and $p_\perp = 0.19$ a.u. ($E_{\boldsymbol{p}} = 5.2\,\mathrm{eV}$). All calculations are performed in the length (solid blue line) and velocity (dotted red line) gauges, leading to the exact same results. In absolute values $\max\mathcal{P}(\varphi) = 2.5$ (a.u.), and $\max|\mathcal{A}(p_\parallel, p_\perp, M)|^2 = 30.8$ (a.u.).

$|\boldsymbol{p}_T(\varphi = 0)| = |\boldsymbol{p}_S(\phi = \pi)|$, as illustrated in Fig. 7. For the parameters considered here we have $p_\parallel = 0.59$ a.u. and $p_\perp = 0.19$ a.u., which correspond to an electron of energy $E_{\boldsymbol{p}} = (p_\parallel^2 + p_\perp^2)/(2m_e) = 5.2\,\mathrm{eV}$. This value, as predicted by the spiral, ensures that the probability of photodetachment is very close to its maximum (see also the top panel in Fig. 2). As before, we perform the calculations in the length (solid blue line) and velocity (dotted red line) gauges. Both gauges lead to the exact same results.

From the top panel of Fig. 8 we see that the probability of detachment is small for twist angles $\varphi < -\pi/2$ and $\varphi > \pi/2$. This is expected, as the circulating momentum approaches the spiral in the interval $\varphi \in [-\pi/2, \pi/2]$. The actual maximum of the distribution is achieved at $\varphi = 0$, when the cone touches the two-dimensional spiral. The OAM distribution (bottom panel) shows that EVSs with topological charges up to $M \approx 28$ units of $\hbar$ (maximum probability) can be generated efficiently. Note that this OAM distribution decreases fast after the maximum is reached.

In Fig. 9 we present the probability distribution as a function of the twist angle (top panel) and the OAM distribution (bottom panel) for $I_{max} = 1 \times 10^{11}\,\mathrm{W/cm^2}$ and $\omega_L = 0.01\,\mathrm{eV}$. While the opening half-angle is still $\beta_T = 0.1\pi$, the parallel and perpendicular components of the twisted momentum are $p_\parallel = 3.09$ a.u. and $p_\perp = 1.0$ a.u., respectively. The energy of photoelectrons is $E_{\boldsymbol{p}} \approx 143.5\,\mathrm{eV}$, which is close

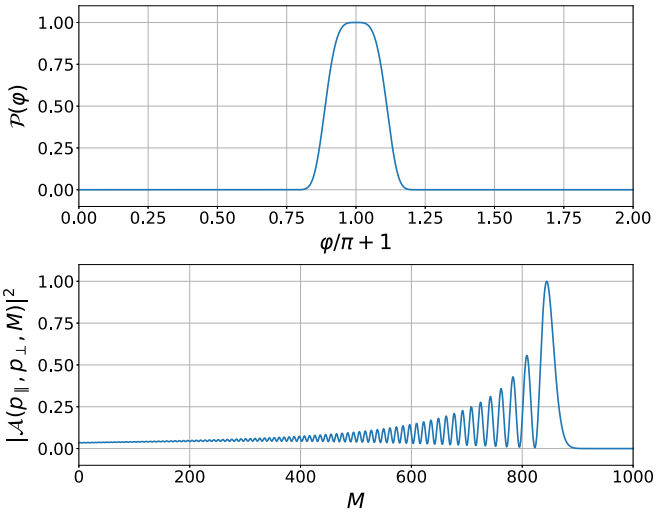

FIG. 9. The same as in Fig. 8, but for the THz driving field (intensity $I_{\max} = 1 \times 10^{11}$ W/cm^2 and frequency $\omega_L = 0.01$ eV). This time, while the half-opening angle remains the same, the parallel and perpendicular components of electron momentum are $p_\parallel = 3.09$ a.u. and $p_\perp = 1.0$ a.u. ($E_p \approx 143.5$ eV). Only the results obtained in the length gauge are shown, as the velocity gauge leads to the exact same dependence. In absolute values $\max\mathcal{P}(\varphi) = 0.1$ (a.u.), and $\max|\mathcal{A}(p_\parallel, p_\perp, M)|^2 = 0.03$ (a.u.).

to the maximum of the probability distribution shown in the bottom panel of Fig. 2. As before, we chose the momentum geometry such that the cone touches the spiral at the laser phase $\phi_0 = \pi$ and twist angle $\varphi_0 = 0$. We present only the calculations in the length gauge, as the velocity gauge gives the exact same results. From the top panel of Fig. 9 we see that the probability distribution as a function of the twist angle $\mathcal{P}(\varphi)$ acquires its maximum values for φ around zero, i.e., when the cone approaches the spiral. For $\varphi < -\pi/4$ or $\varphi > \pi/4$ this distribution is very small, which again corroborates that the probability of photodetachment is substantial only in the vicinity of the spiral. With respect to the OAM distribution (bottom panel of Fig. 9) we observe an oscillating behavior before the maximum is reached. For this particular intensity, it is expected to observe EVSs with angular momentum close to $M \approx 840$ in units of $\hbar$. Hence, by comparing the bottom panels of Figs. 8 and 9 we conclude that EVSs with large topological charges are obtained for smaller driving field frequencies (lower photon energy). This is actually expected, as the electron absorbs a larger number of photons during the ATD process, hence leading to a significantly higher transfer of angular momentum.

An inspection of Figs. 8 and 9 indicates that the OAM distributions have a universal structure: for small values of the topological charge M they oscillate (or show a typical interference pattern), reach the maximum value for a particular M_0, and drop suddenly to zero. In order to explain this behavior, let us go back to the definition (52) and put it in the form

$$\mathcal{A}^G(p_\parallel, p_\perp, M) = \frac{1}{2\pi}\int_0^{2\pi} d\varphi e^{-iM\varphi + i\Phi(\varphi)}|\mathcal{A}^G(\boldsymbol{p}_T(\varphi))|, \tag{53}$$

where $\Phi(\varphi) = \arg\mathcal{A}^G(\boldsymbol{p}_T(\varphi))$. Now, we can analyze this integral by applying the saddle-point approximation. For a given M the main contributions here come from such angles φ_M that satisfy the equation

$$M = \Phi'(\varphi_M), \tag{54}$$

where the prime means the derivative over φ. Since the phase $\Phi(\varphi)$ is defined in the compact interval $[0, 2\pi]$, it has to be bounded. Analysis of the amplitude $\mathcal{A}^G(\boldsymbol{p}_T(\varphi))$ shows (cf., [5]) that, for the considered pulse shape, $\Phi'(\varphi)$ has the maximum for $\varphi = 0$; therefore, $M_0 = \Phi'(0)$. For $M > M_0$ the saddle-point equation does not have real solutions, which leads to the exponential decrease of the OAM distribution. On the other hand, for $M < M_0$, the saddle-point equation has at least two real solutions, which causes the interference of amplitudes calculated for these angles.

V. CONCLUSIONS

Similar to the authors of Ref. [23], we have derived an SFA analytical expression for the laser-induced photodetachment from negative ions with an s valence electron. However, instead of using the saddle-point approximation, we performed numerically the time integrals defining the probability amplitude of detachment. We have centered our attention on the analysis of photodetachment driven by few-cycle laser fields and the generation of EVSs with high topological charges. Note that the SFA is particularly suitable for our calculations, as the photoelectron does not experience the Coulomb tail after it is transferred to the continuum. By making use of the concept of a cone of twisted momentum and extrapolating the idea of an ionization spiral, we have determined the optimal conditions for obtaining EVSs with large probability and topological charges (see also Ref. [5]). The CGPDs allowed us to find the regions in momentum space where the probability of photodetachment is maximal. It is worth mentioning that our theoretical framework is valid provided that the driving field intensity is not too large and the probabilities of detachment per a few field cycles are smaller than 1.

By calculating the energy spectra of photoelectrons for different intensities and frequencies, we have found the appearance of large supercontinua (interference-free structures) which span several tens (or hundreds) of a single-photon energies. The position of such a structure coincides with the predictions arising from the momentum spiral of ionization. Hence, we have shown that such a two-dimensional structure is useful not only in the description of high-energy ionization but also in photodetachment processes for energies larger than the electron affinity.

Our numerical calculations were carried out in the velocity and length gauges independently. For the photodetachment from the $1s$ bound state of the ZRP we have seen that both gauges give identical results, despite the differences in the analytical expressions of the integrands leading to the probability amplitudes [see Eqs. (15) and (19)]. Thus, in accordance with the observations of Gribakin and Kuchiev in [23], we showed that the probability amplitude of detachment is, in fact, gauge invariant. This is not necessarily true for other bound states.

Finally, we have calculated the OAM distribution for photodetachment driven by a circularly polarized, three-cycle laser pulse. For the parameters used in this paper, we have shown that it is possible to obtain EVSs in photodetachment with orbital angular momentum as large as $M \approx 840$ in units of $\hbar$ for $I_{\max} = 1 \times 10^{11}\,\mathrm{W/cm^2}$ and THz fields. A lower frequency of the driving field leads, in general, to higher topological charges.

In closing, we would like to note that generation of propagating EVSs in solid-state materials can open the door to a new type of electronics where, in addition to the electron charge and spin, angular momentum can be transported. It is, in principle, possible to generate EVSs by irradiating negatively doped solids or surfaces by ultrashort THz laser fields of moderate intensity. Additionally, the OAM properties of the resulting vortices can be dynamically controlled by modifying the intensity or frequency of the driving pulse. This could lead, in principle, to investigations of a new type of electron transport in solids or nanostructures, and it is still awaiting deeper exploration.

ACKNOWLEDGMENT

This work is supported by the National Science Centre (Poland) under Grant No. 2018/31/B/ST2/01251.

[1] M. Uchida and A. Tonomura, Nature (London) **464**, 737 (2010).
[2] J. Verbeeck, H. Tian, and P. Schattschneider, Nature (London) **467**, 301 (2010).
[3] K. Y. Bliokh, I. P. Ivanov, G. Guzzinati, L. Clark, R. Van Boxem, A. Béché, R. Juchtmans, M. A. Alonso, P. Schattschneider, F. Nori, and J. Verbeeck, Phys. Rep. **690**, 1 (2017).
[4] S. M. Lloyd, M. Babiker, G. Thirunavukkarasu, and J. Yuan, Rev. Mod. Phys. **89**, 035004 (2017).
[5] F. Cajiao Vélez, K. Krajewska, and J. Z. Kamiński, Phys. Rev. A **97**, 043421 (2018).
[6] K. Krajewska, F. Cajiao Vélez, and J. Z. Kamiński, J. Phys.: Conf. Ser. **1206**, 012002 (2019).
[7] B. M. Smirnov, *Physics of Atoms and Ions* (Springer, New York, 2003).
[8] R. Shakeshaft and X. Tang, Phys. Rev. A **36**, 3193 (1987).
[9] W. Becker, S. Long, and J. K. McIver, Phys. Rev. A **42**, 4416 (1990).
[10] S. Geltman, Phys. Rev. A **43**, 4930 (1991).
[11] C. Blondel, M. Crance, C. Delsart, and A. Giraud, J. Phys. B **24**, 3575 (1991).
[12] M. D. Davidson, H. G. Muller, and H. B. van Linden van den Heuvell, Phys. Rev. Lett. **67**, 1712 (1991).
[13] R. Reichle, H. Helm, and I. Yu. Kiyan, Phys. Rev. Lett. **87**, 243001 (2001).
[14] K. Krajewska, I. I. Fabrikant, and A. F. Starace, Phys. Rev. A **74**, 053407 (2006).
[15] A. Kramo, E. Hasović, D. B. Milošević, and W. Becker, Laser Phys. Lett. **4**, 279 (2007).
[16] K. Krajewska, I. I. Fabrikant, and A. F. Starace, Laser Phys. **17**, 368 (2007).
[17] K. Krajewska, I. I. Fabrikant, and A. F. Starace, Phys. Rev. A **78**, 023407 (2008).
[18] K. Krajewska, I. I. Fabrikant, and A. F. Starace, Phys. Rev. A **86**, 053410 (2012).
[19] T. Andersen, Phys. Rep. **394**, 157 (2004).
[20] L. V. Keldysh, J. Exp. Theor. Phys. **20**, 1307 (1965).
[21] F. H. M. Faisal, J. Phys. B **6**, L89 (1973).
[22] H. R. Reiss, Phys. Rev. A **22**, 1786 (1980).
[23] G. F. Gribakin and M. Yu. Kuchiev, Phys. Rev. A **55**, 3760 (1997).
[24] J.-H. Chen, M. Han, X.-R. Xiao, L.-Y. Peng, and Y. Liu, Phys. Rev. A **98**, 033403 (2018).
[25] M. Dörr, R. M. Potvliege, D. Proulx, and R. Shakeshaft, Phys. Rev. A **42**, 4138 (1990).
[26] I. Žutić, J. Fabian, and S. Das Sarma, Rev. Mod. Phys. **76**, 323 (2004).
[27] J. Z. Kamiński, F. Cajiao Vélez, and K. Krajewska, Laser Phys. Lett. **14**, 075301 (2017).
[28] F. Cajiao Vélez, K. Krajewska, and J. Z. Kamiński, J. Phys. B **51**, 055601 (2018).
[29] F. Cajiao Vélez, J. Z. Kamiński, and K. Krajewska, J. Phys.: Conf. Ser. **999**, 012007 (2018).
[30] D. M. Wolkow, Z. Phys. **94**, 250 (1935).
[31] J. D. Jackson, *Classical Electrodynamics* (Wiley, New York, 1972).
[32] K. Krajewska, F. Cajiao Vélez, and J. Z. Kamiński, *Advances in Optics: Reviews* (International Frequency Sensor Association, Barcelona, 2018), Vol. 2.
[33] K. Krajewska and J. Z. Kamiński, Phys. Rev. A **94**, 013402 (2016).
[34] F. Cajiao Vélez, J. Z. Kamiński, and K. Krajewska, J. Phys.: Conf. Ser. **999**, 012005 (2018).
[35] K. Krajewska, F. Cajiao Vélez, and J. Z. Kamiński, Proc. SPIE **10241**, 102411J (2017).
[36] K. Krajewska, F. Cajiao Vélez, and J. Z. Kamiński, Plasma Phys. Controlled Fusion **61**, 074004 (2019).
[37] A. T. J. B. Eppink and D. H. Parker, Rev. Sci. Instrum. **68**, 3477 (1997).
[38] D. V. Karlovets, Phys. Rev. A **86**, 062102 (2012).